Spatial Distribution of Optical Near-Fields in Plasmonic Gold Sphere Segment Voids

M. Schmidt · N. G. Tognalli · M. A. Otte · M. I. Alonso · B. Sepúlveda · A. Fainstein · A. R. Goñi

Abstract We present a comprehensive experimental and computational study on the electromagnetic field distribution in sphere segment void arrays. Surface plasmon polaritons can be excited in these void arrays, resulting in greatly enhanced electromagnetic fields. With the scanning near-field optical microscope (SNOM) we are able to measure the electromagnetic field distribution at the sample surface. For this purpose, an array of relatively large voids with a sphere diameter of 900 nm was fabricated, allowing for an easy access of the scanning glass-fibre tip and yielding very detailed scans. Complementary, finite-difference time-domain (FDTD) calculations on a complete void array have been performed and compared with the SNOM intensity maps and experimental reflectivity data. We show in a direct way both the existence of extended and localised modes in the Au void array for three different void depths. We also show and discuss the changes that the modes undergo for the different void depths and excitation wavelengths. Moreover, since the simulations were performed for two different void geometries, one containing perfectly spherical void surfaces and another more realistic one, which considers the presence of interstitial wall holes and other imperfections, as observed in scanning electron micrographs, we were able to determine by comparison with the experiment under which conditions an array of idealised sphere segment voids is a meaningful model. This demonstrates that both SNOM and FDTD simulations are powerful tools for understanding the plasmonic response of metallic nanostructures, thus enabling, for instance, a design for applications in ultra-sensitive optical detection.

Keywords Scanning near-field optical microscope · Plasmonic nanostructure · Finite-difference time-domain calculation

M. Schmidt (✉) · M. I. Alonso · A. R. Goñi (✉)
Institut de Ciència de Materials de Barcelona (ICMAB-CSIC),
Campus de la UAB, Bellaterra, 08193 Catalunya, Spain
e-mail: mschmidt@icmab.es,
e-mail: goni@icmab.es

N. G. Tognalli · M. A. Otte · B. Sepúlveda
Research Center on Nanoscience and Nanotechnology
(CIN2-CSIC) & CIBER-BBN,
Bellaterra, 08193 Barcelona, Spain

A. Fainstein · N. G. Tognalli
Centro Atómico Bariloche-Instituto Balseiro, C.N.E.A.,
8400 San Carlos de Bariloche, Río Negro, Argentina

A. R. Goñi
ICREA, Passeig Lluís Companys 23, 08010 Barcelona, Spain

Introduction

The field of plasmonics has attracted a lot of interest in recent years, because of the potential applications in optical switching [1], near-field photonics [2], photovoltaics [3], surface plasmon resonance [4–7] and surface-enhanced Raman scattering (SERS) [8–16]. In the past decade, substrates consisting in sphere segment void arrays were developed by Bartlett et al. [17, 18]. These kinds of substrates can be produced with large spatial homogeneity, repeatability and time stability, providing, in addition, a great control over the plasmon mode frequency which can be tuned in a wide spectral range, from the visible to the near infrared [19–31]. The sphere segment void structures are widely used to detect the faint Raman signal of molecules in biosensors via SERS

[31–34] and were also suggested to be suitable for enhancing photovoltaic efficiencies [3, 35, 36]. In both cases, a good understanding of the electromagnetic field distribution generated by excitation of surface plasmon polaritons in these substrates is of crucial importance. However, our knowledge relies first and foremost on results of theoretical studies of idealised structures or reflectivity measurements, since direct measurements of the optical near-field distribution are scarce [24, 37, 38]. For a direct determination of such electromagnetic field distribution, the use of a scanning near-field optical microscope (SNOM) is particularly suitable, as it probes the sample directly at the surface in the exponentially decaying near-field of the surface plasmon polaritons.

In a previous work [24], we have successfully investigated an array of gold spherical voids by means of SNOM, directly mapping polariton intensity distributions inside voids of 600 and 800 nm in diameter excited with different photon energies. Although the overall picture obtained from these measurements compared well to reflectivity results and theoretical calculations regarding the field distribution inside single Au voids, the topography line-scan profiles across any void exhibited a funnel-like shape, clearly indicating that the SNOM probe was not able to follow the concave spherical shape of the voids with complete fidelity. Moreover, a preliminary study of the obtained substrates using scanning electron microscopy (SEM) shed further light on the actual shape of the voids, which close to the bottom of the void appeared to be flat rather than perfectly spherical. In order to investigate the importance of all these issues, we improved the accessibility of the scanning probe by fabricating a sample with larger spherical voids of 900 nm in diameter, having terrace-like zones with different void depths ranging from a flat surface to almost complete closure of the spheres. Additionally, we now compare the SNOM images with results of finite-difference time-domain (FDTD) calculations in realistic sphere segment void arrays, which are able to account for the spatial distribution of the electromagnetic field associated to both localised and extended plasmon modes in a single computational run. As the simulations model an experiment with excitation with plane-wave light at normal incidence, the comparison to the experiment is rather straightforward. The calculated field intensity distribution can be compared to the near-field spatial distribution obtained by SNOM, while the calculated power flux through a surface above the array can be related to spectra measured in reflectivity experiments. A key feature of our FDTD simulations is that, in addition to an array of perfectly spherical voids, we calculated the near-field distribution considering a more realistic void geometry which contains several kinds of imperfections such as the flat bottom and wall holes that form between voids at large void depths, as observed in the SEM images. This gives the unique opportunity to investigate the impact of a departure from a spherical surface shape on the spatial distribution of the surface plasmon polaritons excited in each particular case.

In order to assign the features observed in the experiments as well as the FDTD calculations to certain excited modes, we made explicit use of the results obtained by Kelf et al. [21] and Cole et al. [22] from calculations that use the boundary element method (BEM) to solve the eigenvalue/eigenvector problem of single voids. As a general behaviour, it is expected that localised or Mie-like modes are excited inside the curved surface of each individual void, being bound to them. In contrast, the so-called Bragg modes extend over the whole remaining flat region of the substrate and couple to light by the grating effect induced by the regular pattern of voids. Therefore, localised modes would depend on the form and size of the void, whereas Bragg modes would be mainly affected by the periodicity of the array, amount of surface roughness and the light incidence angle.

Experimental Details

The nanovoid arrays are fabricated via a hexagonal close-packed self-assembly of polystyrene spheres (Duke Scientific Corporation) with diameters of 900 nm followed by an electrochemical Au deposition (TG-25 RTU, Technic Inc.) [17]. During this process, a 1 % aqueous solution of nanospheres fills a thin cell made of a cysteamine-modified gold-coated glass slide, a clean glass slide and sidewalls made of a 300-μm-thick spacer of Parafilm. The gold coating is approximately 100 nm in thickness. The cysteamine monolayer is incorporated to facilitate the filling of the thin cell and to reduce the contact angle of the aqueous solution on the surface. This forms a sweeping meniscus tail as the fluid dries, which pulls spheres to the evaporation line, where they form a close-packed monolayer domain. After the self-assembly of the polystyrene template, the sample is immersed into an electrochemical plating bath. The void depth t, defined as the ratio between the depth of a void and the sphere diameter, is determined by controlling the deposition rate and time. Moreover, by systematically retracting the sample every 500 μm from the electrochemical bath during the metal deposition, it is possible to achieve different void depths in one single graded sample. Finally, the sample is sonicated in dimethylformamide to remove the polystyrene template. The final result of the process can be seen in the SEM images presented in Fig. 1. Figure 1a shows that a reproducible and well-defined hexagonal array of Au voids with a diameter of 900 nm is obtained. The other pictures in Fig. 1 (varying void depth) were taken at an angle of 45° and demonstrate that, through the variation in

Fig. 1 SEM images of the sample surface. **a** top view and **b–f** at 45° for different void depths of approx. **b** $t = 0.15$, **c** $t = 0.35$, **d** $t = 0.5$, **e** $t = 0.7$, **f** $t = 0.9$. The void depth t is defined as the ratio between the depth of a void and the sphere diameter
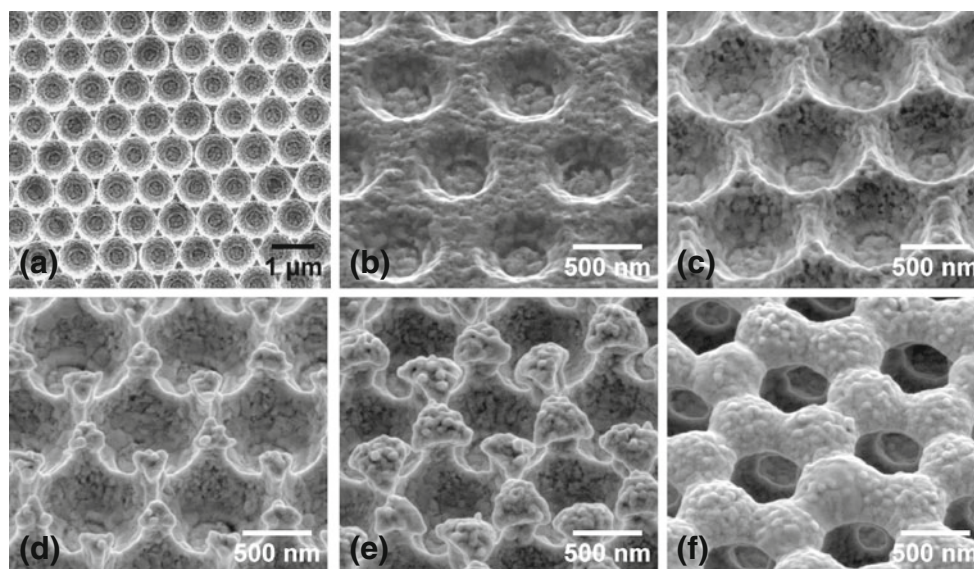
deposition time, the same high array quality is maintained over all void depths, e.g. from the very shallow voids with $t \approx 0.15$ shown in Fig. 1b up to nearly complete coverage (see Fig. 1f, $t \approx 0.9$). These t values were approximately determined by the geometrical appearance of the voids in the SEM images. It is clear that the actual shape of the voids fabricated by this method departs from that of an idealised spherical void array, which might influence its plasmonic properties. We see that one of the most severe differences with a perfect sphere involves the bottom of the voids that appear flat. Another very important difference concerns the areas where the voids are interconnected, leaving isolated pillars instead of closed walls (see, for instance, the circular interstitial holes in the walls between two adjacent voids in Fig. 1f). This is probably a consequence of the poor wetting of the aqueous solution in regions where the polymer spheres touch the surface of the substrate and where they touch each other, preventing the efficient gold deposition in these regions during electrochemical plating. Additionally, one observes in the SEM images that the deposition method introduces a certain amount of surface roughness. It is still a matter of discussion to what extent this can influence the surface plasmon polaritons.

The near-field intensity patterns were recorded with a Veeco Aurora-III system equipped with a photomultiplier detector. The SNOM probe was operated in shear-force feedback conditions with a tuning-fork working at 100 kHz and keeping a constant probe-to-sample distance of about 10 nm during scans. All measurements were performed in reflection–collection mode, in which the illumination takes place at an angle of incidence of 45° by focusing the light on the sample with a ×20 microscope objective and the near-field signal is collected by the SNOM tip. The glass-fibre tips are coated with an opaque layer of fine-grained

aluminium and have an aperture of about 100 nm. In this way, we attained sub-wavelength spatial resolution better than 80 nm. Three different laser wavelengths were available for excitation: the 515-nm line of an Ar-ion laser, the 633-nm line of a He–Ne laser and the 785-nm line from a solid state laser. The far-field excitation was predominantly s-polarised. Our feedback mechanism allows us to obtain a topographical image of the sample simultaneously with the optical one. In the measurements, we avoided retracting the tip when changing the wavelength of the illumination, so that for each colour, exactly the same voids have been measured under the same conditions. In addition, reflectivity measurements have been performed with a Sopra GES5E ellipsometer with s-polarised light from a xenon lamp and at 45° incidence, i.e. under similar conditions as for the SNOM experiments. All optical measurements were carried out at room temperature.

Electrodynamics Simulations

The simulations have been performed with the commercially available program Lumerical, which solves Maxwell equations in time domain by the method of finite-differences. The system under theoretical study consists in a perfect hexagonal array of Au sphere segment voids. The hexagonal void array was modelled according to the SEM images of Fig. 1 and the topographical information obtained from the SNOM measurements. This was done in one case by considering an idealised void shape of perfect sphere segments and in another case by accounting for the void interconnections and flat bottom of the voids in form of circular holes. In order to treat the whole array rather than just one single void, one needs to consider periodic boundary

conditions at the borders of the simulation volume. Because of limitations of the computational code, the use of periodic boundary conditions as well as an illumination with *white* light at a well-defined angle restricted us to the use of normal incident light. This would still yield a good approximation for the spatial distribution of the Mie-like modes even though the experiments were carried out at 45° incidence [3, 21]. Thus, for the comparison with the experiment one has to keep in mind that the strength exhibited by different plasmon polariton modes depends on the mutual orientation of their dipolar moment and the polarisation vector of the incident light and consequently also on the angle of incidence [22]. Moreover, one has to take into account that energy dispersive modes such as propagating Bragg modes shift in frequency for excitation at different angles [21]. Finally, the spatial distribution is analysed at selected cross-sectional planes of the void array structure for the wavelengths of the lasers used in the SNOM experiments.

Results and Discussion

We first present the results of reflectivity measurements and compare them to the FDTD spectra and pertinent literature work, in order to interpret the observed features and provide a tentative mode assignment. The latter is important for a better understanding of the optical near-fields mapped out in SNOM experiments, when compared to the field intensity distributions obtained from the FDTD calculations. In particular, we take a closer look at the dependence of the near-field distributions on void depth t and excitation wavelength associated with the surface plasmon polariton mode excited in each case.

Figure 2 shows the reflectivity measurements (left panel) and the simulated reflectivity spectra (right panel) for various void depths between $t = 0$ and $t = 1$. Here, the simulations were performed using perfectly spherical voids. The SEM measurements (see examples in Fig. 1) were used to estimate the listed values of t for the reflectivity measurements, according roughly to a system of positional marks established on the sample. This made possible a comparison between the results of different experiments and the simulations as well. The measured and calculated reflectivity show very similar features over the entire range of t values. For low void depths, the reflectivity spectra exhibit the typical edge-like line shape of flat gold (topmost spectrum), where the sharp decrease in reflectivity at around 500 nm is due to interband optical transitions involving d-electrons in Au [39, 40]. The ragged signal at long wavelengths observed in the measured spectra for very low t is an artefact caused by the incomplete signal correction of high intensity peaks from the xenon lamp. As the void depth increases, we observe two effects: on the one hand, the overall reflectivity decreases
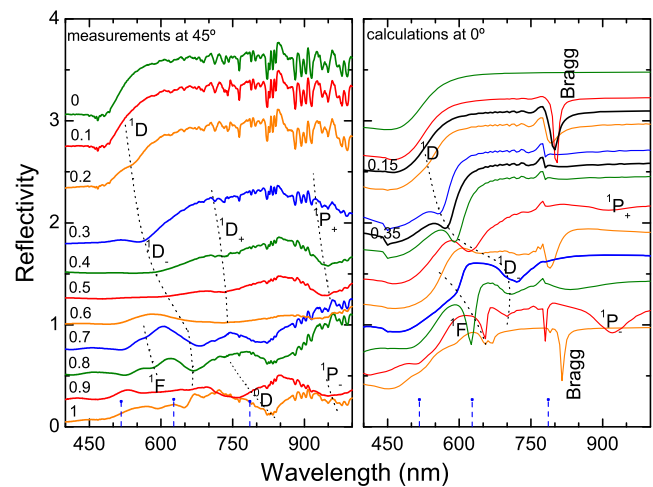

Fig. 2 In the *left panel*: measured reflectivity for several approximate void depths between 0 and 1 for s-polarised light at an angle of 45°. In the *right panel*: the corresponding simulated reflectivity at normal incidence with two additional void depths of $t = 0.15$ and $t = 0.35$ for the comparison with the SNOM measurements. All graphs are displaced 0.25 units every $0.1t$. The three available laser lines for SNOM measurements are marked by the *short vertical lines*

on account of the increased corrugation of the reflecting surface. On the other hand, a rich structure of relatively broad dips is apparent in the spectra at different wavelengths, depending strongly on t. These dips in reflectivity are attributed to the absorption of electromagnetic radiation due to the excitation of different plasmon polariton modes characteristic of nanostructured metallic surfaces [21].

We now proceed with the assignment of the observed reflectivity features to extended (Bragg) as well as localised (Mie-like) modes, according to the variation of their frequency with void depth. Extended Bragg modes are fairly insensitive to changes in the depth of the voids as long as the periodicity of the array is conserved. The absorption dip at 800 nm in the calculated spectra is assigned to a Bragg mode, according to a study by Kelf et al., in which the Bragg modes appear at this wavelength for normal incidence [21]. This mode is clearly visible in the simulated spectra only for t values for which there is an appreciable amount of flat area between the voids, i.e. for very thin and very thick films. The Bragg modes, which should be centred at 750 nm and 500 nm for an angle of incidence of 45° [21] are absent in the measured spectra most likely because such extended modes are totally damped (highly broadened) by surface roughness. On the contrary, the frequency of Mie-like modes, which are localised in the voids, depend strongly on the degree of truncation. Following previous works [22, 29] and adopting the mode labelling $^mL =^{0,1,...}$ $P, D, F, ...$ [22] in terms of the quantum numbers of atomic orbitals, which complies with the spherical symmetry of the voids, we propose the mode assignment, as indicated in Fig. 2 (dotted curves are a guide to the eye). All localised

modes shift to longer wavelengths with increasing t values, as expected [22, 29]. The ^1D mode which for low t appears at about 550 nm splits at around $t = 0.3$ noticeably into a $^1D_+$ and a $^1D_-$ doublet. This splitting is due to a coupling of the ^1D mode to a so-called rim dipole mode, which exists only in the truncated voids [22]. Several absorption dips at around 500 nm are apparent for $t \geq 0.5$ and are interpreted as F modes, moving to longer wavelength as the voids are less truncated. According to BEM calculations [22], these F modes should exhibit strong and narrow absorption dips, as observed in our experiments and reproduced by our calculations. In contrast, P modes are observed at around 950 nm, far away from the three available laser lines. In our simulations, the illumination at normal incidence precludes the observation of modes with $m = 0$ such as ^0P and ^0D. These modes are, nevertheless, very little pronounced in the experiment as well. We can only infer their presence at very high t values. Finally, we remark that we have measured the dispersion of the modes observed in reflectivity (not shown) for a few t values (0.15, 0.3 and 0.75) by varying the incidence angle between 25 and 75°. Most of the observed dips do not show any appreciable dispersion, in agreement with their interpretation as localised Mie-like modes. Nevertheless, we find faint modes centred at around 650 nm for $t = 0.3$ and at around 800 nm for $t = 0.75$, which exhibit clear shifts to shorter wavelengths with increasing incidence angle below 45°, in accordance with the FDTD predictions for the appearance of Bragg modes in reflectivity (see Fig. 2).
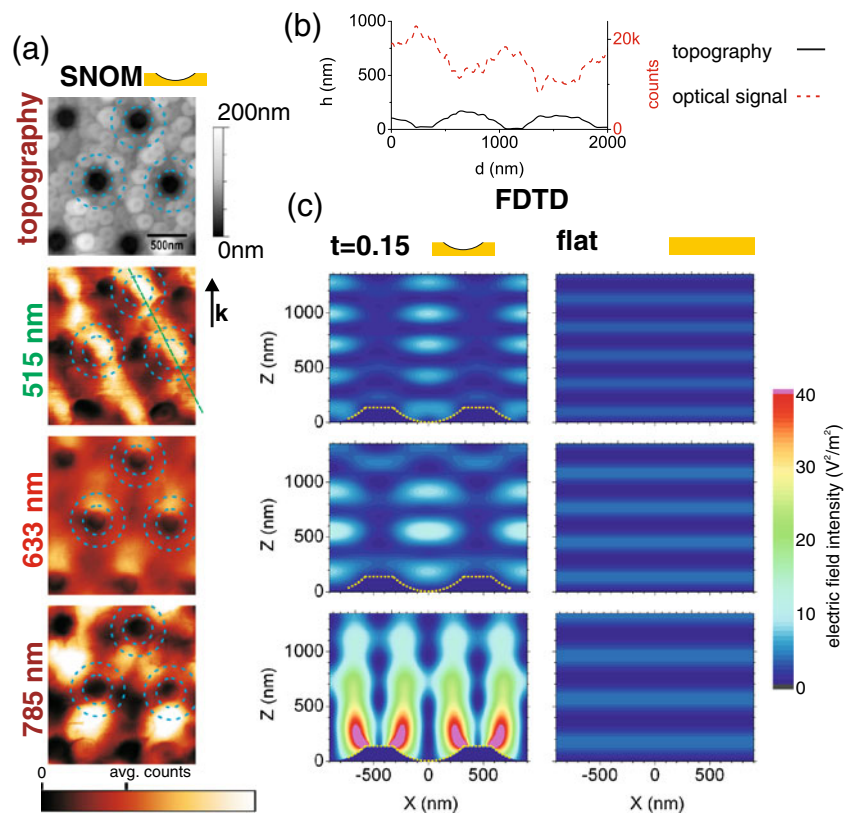
Having assigned the different plasmon modes observed in reflectivity experiments, we now turn to the discussion of the SNOM data, making a comparison with the electric field distributions obtained from the FDTD simulations. We have chosen for that purpose three representative truncation degrees: $t = 0.15$, $t = 0.35$ and $t = 0.7$. Figure 3 shows the results of the SNOM measurements and the FDTD simulations side by side for $t = 0.15$ for the three excitation wavelengths at 515 nm, 633 nm and 785 nm (from top to bottom). In Fig. 3a and in all SNOM images throughout this paper, the inner circle marks the position of the *inner* rim of each void corresponding to the flat bottom, whereas the outer circle denotes the *outer* border of the void at the plane of truncation. The black arrow indicates the direction of the light. The shown topography image corresponds to one of the SNOM measurements. Since the other two topography images are almost identical, we slightly adapted the optical images in order to make the comparison straightforward between all excitation wavelengths. In spite of its lower resolution, the topography sensed by the SNOM tip reproduces very well the SEM images obtained for the sample. We emphasise that the SNOM measurements were performed consecutively by changing the excitation wavelength without retracting the tip from its feedback position.

The changes observed in the SNOM pictures are therefore caused only by the use of another illumination source. The intensity scale of each optical image has been normalised to its average intensity as indicated by the colour scale. Figure 3b displays a typical line profile of both SNOM and topography signals along the dashed green line marked on the image of Fig. 3a for the 515 nm excitation. From the topographical information, we can infer that the SNOM tip enters the voids very well; even the flat region at the bottom is clearly apparent. This allowed, in addition, for a precise determination of t by the measured depth.

The SNOM images clearly change with the excitation wavelength showing that the near-field distributions depend on the particular modes being excited at a given energy. Strong features are observed outside the voids, which we attribute to extended (Bragg) modes. For this truncation degree, they have a relatively large flat area to propagate on and, thus, a relatively high intensity. Nevertheless, one has to keep in mind that in nanostructures like the void arrays, a comparison of the SNOM intensities outside and inside concave areas needs to take shadowing effects into account, occurring when the tip enters a void. According to their dispersion behaviour, we expect Bragg modes to be approximately resonant at 45° for 515 nm and 785 nm but not for 633 nm excitation [21]. For 515 nm the SNOM, intensity is distributed in a sort of diagonal stripe pattern along the planar region going through the voids. Additionally, we expect for this wavelength to observe the ^1D Mie-like mode localised at the voids [22]. Indeed, the profile in Fig. 3b indicates that the near-field intensity is highest within the void. Moreover, we want to emphasise the fact that Bragg modes can be sensed by SNOM even though they are not detected in the reflectivity measurement. This shows the importance to investigate the near-fields directly instead of deducing the existence or non-existence of surface plasmon polaritons exclusively from far-field measurements. Apart from the just explained modes, the image for 515 nm (and to some extent also 785 nm) exhibits dark spots, which do not correlate with the voids but with grains on the surface. The dark spots are thus probably caused by these grains disturbing the propagation of the Bragg modes. For the 633 nm excitation, the image shows much less pronounced near-fields, which confirms the expected poor excitation efficiency of extended as well as localised modes. For 785 nm, the excited Bragg mode produces again a strong signal on the flat surface of the sample. The observed pattern is different from that for 515 nm, for the excited modes are different. The deep black voids are in accordance with the absence of Mie-like modes for that wavelength.

We turn to the discussion of the FDTD calculations for the same t value of 0.15. Results are presented in Fig. 3c as intensity plots for a cross section through the middle of

a void together with the calculations for flat gold. We note that these are the very same calculations that we have presented in Fig. 2 showing the reflectivity spectra, thus, any absorption feature seen in the latter should have its counterpart in the images of the near-field distribution, related to a plasmon polariton excitation. Above the surface of the void array but belonging to the far-field region, a spatially modulated electromagnetic field is obtained from the calculations. Its origin becomes clear when looking at the results for flat gold (right panel), where this modulation exists as well. The incident light and its reflection from the flat gold surface form together a standing wave above the surface with a node at the gold/air interface and further nodes spaced by $\lambda/2$. Therefore, in the calculation for $t = 0.15$, we also have a standing wave, though influenced by the presence of the voids. This standing wave does not affect the field associated with the surface plasmon polaritons, on which we focus our attention from now on. In comparison with the SNOM measurements, the simulations for 515 nm also show a high near-field strength close to the surface inside the voids (dashed yellow line) with a spatial distribution characteristic of a dipole-like ^1D mode [22]. For the 633 nm excitation, the electric field stems mostly from the standing wave and not from a Mie-mode and, therefore, close to the surface, the field intensity is very low. As the SNOM tip probes the electric field close to the substrate surface,

this difference is very important and our calculations confirm nicely the low signal measured for 633 nm inside the voids. Also in agreement with the SNOM measurements, the calculation for 785 nm excitation shows no strong fields from Mie-like modes within the voids. The higher intensity regions calculated for this wavelength are more at the void rims formed with the upper flat surface. This feature stems from the resonance with the aforementioned Bragg modes at 800 nm (right panel of Fig. 2) [21].

As we increase the void depth to $t = 0.35$, the response of the system to the illumination changes drastically. The SNOM images in Fig. 4a show abundant and very well-resolved features inside the voids indicating that the deeper the voids, the stronger the local modes. For all excitation wavelengths, we see bright features around the inner dashed circle; this observation agrees well with the expected character of ^1D-like modes. It is important to mention that a possible polarisation scrambling of the predominantly s-polarised light causes modes to appear smeared out in all directions. From a closer look to the case of 515 nm excitation, we infer that the centre of the void (within the inner dashed ring) remains rather dark, whereas for 633 nm excitation, it exhibits a strong field close to the centre. For 785 nm, we observe a remarkably strong signal around the edges (between the two dashed circles) and outside the voids. This can be explained by the previously

mentioned $^1D_+$ mode, a ^1D mode that would couple to the rim mode with the same field orientation [22]. This mode is expected to be resonant with 785 nm light and gives rise to a high field intensity about the rim area. The intensity distribution at the inner dashed circle shows a similarity to the ones for 633 nm but are slightly rotated and are thus probably due to the $^1D_-$ mode (the ^1D and the rim mode have opposite field orientations), which is excited at that wavelength. The profiles in Fig. 4b along the dashed lines in the SNOM maps for 633 nm and 785 nm clearly show the similarity of the field distribution in the centre of the void. This mode might therefore have a rather broad energy distribution in our sample. The SNOM measurement shows also outside the voids a great change compared to the t value of 0.15. This suggests the absence of those Bragg modes, supported also by the disappearance of the Bragg absorption dip in the simulated reflectivity spectrum of Fig. 2. Moreover, note that in real samples, the growth of the pillars sets in (SEM image in Fig. 1c) disturbing the propagation

of the Bragg modes on the connected flat surface around the voids.

We now turn our attention to the calculations for this void depth presented in Fig. 4c and their comparison with the SNOM measurements. The calculations show a dipole-like field distribution along the light polarisation vector for each excitation wavelength. The two lobes change from a more connected form for 515 nm and 633 nm to a one with the lobes separated from each other and close to the rim for 785 nm. For 515 nm and 633 nm excitation, the calculations agree well with the measurement and even confirm that at the surface, the field distribution for 633 nm is concentrated close to the centre, while for 515 nm, the central region exhibits relatively low field intensities. For 785 nm, the electric field is observed in both the calculation and the measurement with a similar spatial distribution.

Finally, we discuss the results obtained for the void depth of $t = 0.7$. Figure 5 shows the SNOM data and the calculated electromagnetic field distribution for this case. The isolated pillars begin to grow towards the centre of the voids, which prevents the tip from deeply penetrating the voids as well as from approaching the walls of the voids. For all three excitation wavelengths, the protruding pillars exhibit a strong localised plasmonic response (Fig. 5a). The upper parts of the pillars come so close that for 633 nm and 785 nm, very intense fields are created between two pillars, if and only if they are arranged along the polarisation of the light. This is a well-known phenomenon for metallic nanoparticles, where these so-called "hot spots" are created between them [41]. This excitation is likely to cause the absorption dip around 800 nm in the experimental reflectivity (Fig. 2). The field distribution inside the voids is also clearly wavelength-dependent but the differences in the spatial distributions are less marked than for the shallower voids. In order to elucidate the measured field distribution, we first discuss the one predicted by the calculation in Fig. 5b. The left panels show the results of the calculations for perfectly spherical voids. The calculation predicts the existence of clearly resolved electric fields inside the voids. The triangular arrangement of the field intensity inside the void for 515 nm excitation confirms the expected F-like mode. For the other two wavelengths, the dipole-like field distribution in the lower part of the void can be explained by ^1D-like modes. For comparison with the SNOM data, it is important to estimate where the SNOM tip probes the electric field inside the void. The dashed red line corresponds to the inferred path of the tip on the basis of a real scan taken from the topography data. Following that path, we expect to see for 515 nm a strong signal in the central part of the void, depending on the exact path possibly also more in a dipole-like form. For 633 nm and especially for 785 nm, we expect an extended strong signal inside the voids. While for 515 nm, this can explain
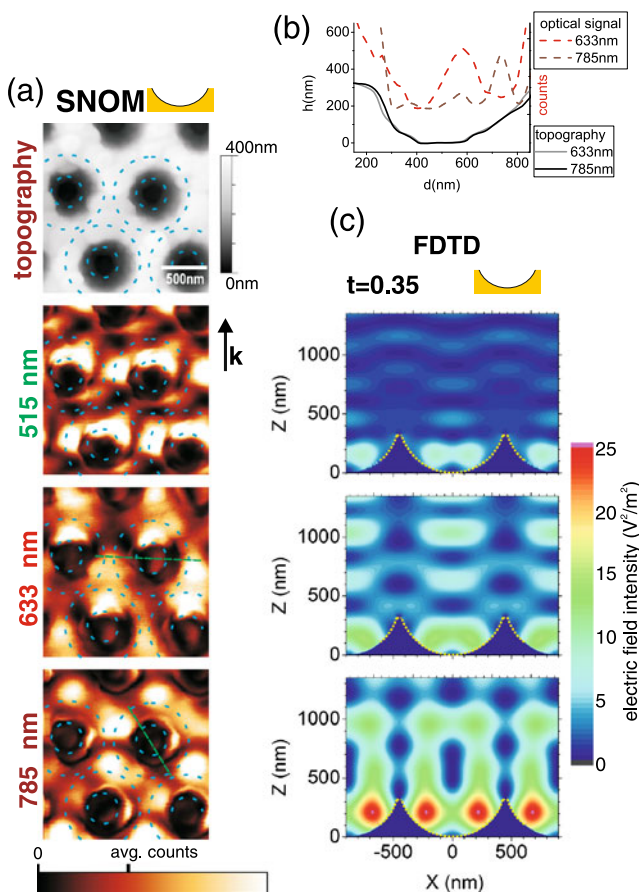

Fig. 4 SNOM measurements and FDTD calculations for $t = 0.35$. **a** SNOM topography and optical maps (average intensities in maps: 1192 counts (515 nm), 1169 counts (633 nm) and 741 counts (785 nm)). **b** Profile for 633 nm and 785 nm as indicated in (**a**) by *dashed lines*. **c** Field intensities in the FDTD calculation

Fig. 5 SNOM measurements and FDTD calculations for $t = 0.70$. **a** SNOM topography and optical maps (average intensities in maps: 1121 counts (515 nm), 867 counts (633 nm) and 1056 counts (785 nm)). **b** FDTD calculations for spherical and non-spherical voids. The *dashed red line* marks the idealised path the SNOM tip has taken in the corresponding measurement
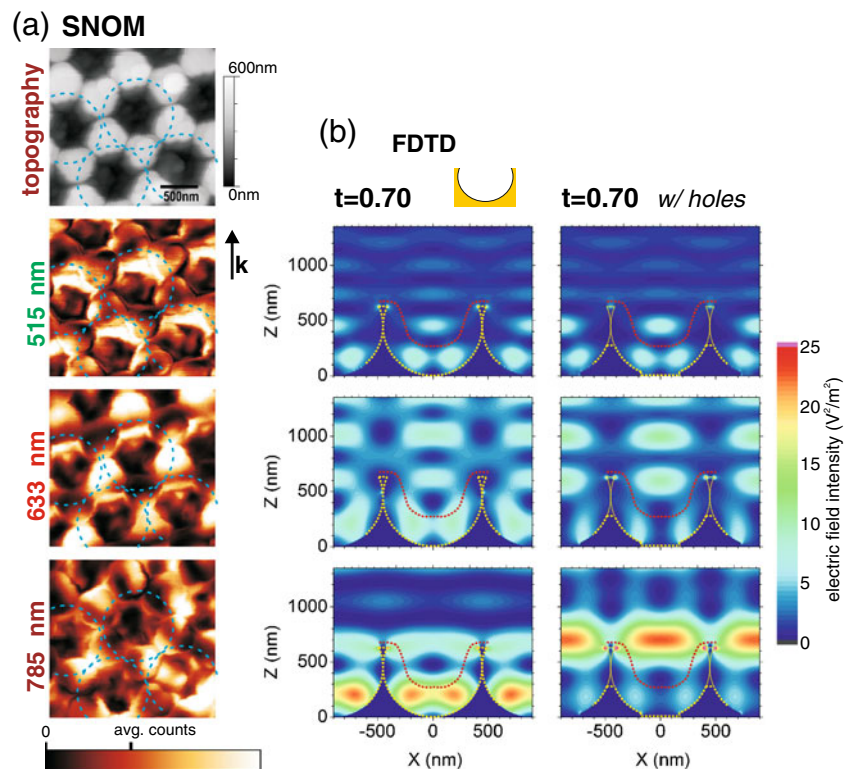
the measurement to a satisfactory degree, there is a clear discrepancy between the calculations and the measurement for the other two wavelengths. This led us to the conclusion that the idealised model of perfectly spherical voids is not realistic enough.

As explained earlier, the real voids have a flat bottom and, more importantly, for void depths larger than $t = 0.5$, there are large circular holes at the walls connecting two adjacent voids. In order to examine what effect this has on the near-field distribution, we performed the same calculation as before but with a more realistic morphology including circular holes with a diameter of 350 nm at the bottom and the walls. The resulting field distribution is shown on the right panels of Fig. 5b, and it is clear that the difference to the idealised case is quite significant. For 515 nm, the electric field remains virtually unchanged in shape and intensity inside the void. However, for the other two wavelengths, a stronger electric field at the opening of the void is expected, whereas the electric fields ascribed to the localised ^{1}D-like mode are weakened and pulled away from the centre. As a result, in the measurements for 633 nm, we still expect a strong signal on the path of the SNOM tip but pushed away from the centre, whereas for 785 nm, the relatively weak fields at the bottom of the void can be expected to give just a low SNOM intensity contrasting with the comparatively strong intensity at the void border. This pattern of the more realistic model coincides much better with the measured

field intensities. Considering the difficulties connected with measuring such deep voids, this qualitative agreement is a satisfactory result. Furthermore, it draws attention to the significance of taking into account the pillar structure correctly when predicting the field strength inside the voids.

The discussion showed altogether quite good agreement between the SNOM measurements and our calculations as well as the literature results, but, of course, one has to be careful to what extent a direct comparison is possible. It is definitely encouraging that the calculations and the measurements agree in so many points, for it shows that we can rely to a certain extent on the calculations in order to predict the excited surface plasmon polaritons inside as well as outside the voids. And for the experiment, it also means that the tip is most probably not changing the modes qualitatively and therefore this technique appears to be reliable to map out the spatial distribution of both the Bragg as well as the Mie-like plasmons. We have shown with our SNOM system that for easily accessible (protruding) structures like in the case of nanowires, the disturbing influence of the tip is low and an excellent agreement between measurements and calculations is obtainable [42], but in the present case, there could be a certain influence of the tip at least within the voids [41]. Thus, some modes might be seen weaker than they are without the tip or possibly they are perceived slightly distorted. It would be very interesting for a deeper study to perform simulations at the same angle as the SNOM

measurement and to take into account the measuring tip in order to clarify further how calculations and experiment can be compared best. Concerning, for example, the connection between the voids, Romero et al. calculated that a new mode appears with a high intensity between the voids [43, 44]. As the discussion for the last case of $t = 0.7$ showed very well, this geometrical change is even more important for open void structures and that accounting for this complexity yields a significantly more realistic field distribution. On the contrary, the flat bottom part, though being a considerable deviation from the idealised spherical void, appears to have only a small effect of "pulling" the electric fields slightly towards the edge of the bottom hole (as shown in Fig. 5b).

Conclusions

We have combined several experimental techniques such as SEM, SNOM and optical reflectivity together with FDTD computational calculations to study in detail the plasmonic response of gold sphere segment void arrays. The measurements were carried out on a thickness-graded void array sample with voids of 900 nm in diameter as a function of its truncation degree and of the incident laser wavelength. We compared the experimental results with the FDTD simulations accounting for both localised (or Mie-like) and propagating (or Bragg) surface plasmon polaritons. For relatively flat arrays with void depths roughly $t < 0.5$, a good agreement was achieved between experimental and computational results for a spherical void shape, being able to assign both localised Mie-like and extended Bragg modes and to explain their behaviour as a function of void depths. For deeper void structures, in contrast, the clear departures from a perfectly spherical void shape, as detected in SEM, ought to be considered and accounted for within the simulations in order to understand the near-field distributions associated to different plasmon polariton modes measured by SNOM. Our findings highlight that both SNOM and FDTD simulations are powerful tools for the study, understanding and also prediction of the electromagnetic response of purposely-designed nanostructured plasmonic substrates.

References

1. Krasavin AV, Zayats AV, Zheludev NI (2005) J Opt A Pure Appl Opt 7(2):S85
2. Zayats AV (2003) Smolyaninov, II. J Opt A Pure Appl Opt 5:S16
3. Lal NN, Soares B, Sinha JK, Huang F, Mahajan S, Bartlett PN, Greenham NC, Baumberg JJ (2011) Opt Express 19(12):11256. doi:10.1021/nl101875t.8
4. Otte MA, Sepúlveda B, Ni W, Perez Juste J, Liz-Marzán LM, Lechuga LM (2010) ACS NANO 4(1):349. doi:10.1021/nn901024e
5. Otte MA, Estévez MC, Regatos D, Lechuga LM, Sepúlveda B (2011) ACS Nano 5(11):9179. doi:10.1021/nn203432z
6. Lechuga LM (2005) In: Gorton L (ed) Biosensors and modern biospecific analytical techniques. Elsevier Science
7. Sepúlveda B, Angelomé PC, Lechuga LM, Liz-Marzán LM (2009) Nano Today 4(3):244. doi:10.1016/j.nantod.2009.04.001
8. Tian ZQ, Ren B, Wu DY (2002) J Phys Chem B 106(37):9463
9. Etchegoin P, Maher RC, Cohen LF, Hartigan H, Brown RJC, Milton MJT, Gallop JC (2003) Chem Phys Lett 375(1–2):84. doi:10.1016/S0009-2614(03)00821-2
10. Freeman RG, Grabar KC, Allison KJ, Bright RM (1995) Science 267(5204):1629. doi:10.1126/science.267.5204.1629
11. Kiely CJ, Fink J, Brust M, Bethell D, Schiffrin DJ (1998) Nature 396(6710):444. doi:10.1038/24808
12. Felidj N, Aubard J, Levi G, Krenn JR, Salerno M, Schider G, Lamprecht B, Leitner A, Aussenegg FR (2002) Phys Rev B 65(7). doi:10.1103/PhysRevB.65.075419
13. Jackson JB, Westcott SL, Hirsch LR, West JL, Halas NJ (2003) Appl Phys Lett 82(2):257. doi:10.1063/1.1534916
14. Kelly KL, Coronado E, Zhao LL, Schatz GC (2003) J Phys Chem B 107(3):668. doi:10.1021/jp026731y
15. Dick LA, McFarland AD, Haynes CL, Van Duyne RP (2002) J Phys Chem B 106(4):853. doi:10.1021/jp0136381
16. Tognalli NG, Fainstein A, Calvo E, Bonazzola C, Pietrasanta L, Campoy-Quiles M, Etchegoin P (2005) J Chem Phys 123(4). doi:10.1063/1.1954707
17. Bartlett PN, Birkin PR, Ghanem MA (2000) Chem Commun 17:1671. doi:10.1039/b004398m
18. Coyle S, Netti MC, Baumberg JJ, Ghanem MA, Birkin PR, Bartlett PN, Whittaker DM (2001) Phys Rev Lett 87(17):176801
19. Netti MC, Coyle S, Baumberg JJ, Ghanem MA, Birkin PR, Bartlett PN, Whittaker DM (2001) Adv Mater 13(18):1368
20. Kelf TA, Sugawara Y, Baumberg JJ, Abdelsalam ME, Bartlett PN (2005) Phys Rev Lett 95(11):1. doi:10.1103/PhysRevLett.95.116802
21. Kelf TA, Sugawara Y, Cole RM, Baumberg JJ, Abdelsalam ME, Cintra S, Mahajan S, Russell AE, Bartlett PN (2006) Phys Rev B 4(24):245415
22. Cole RM, Baumberg JJ, García de Abajo FJ, Mahajan S, Abdelsalam ME, Bartlett PN (2007) Nano Lett 7(7):2094
23. Teperik TV, Popov V, García de Abajo FJ, Abdelsalam ME, Bartlett PN, Kelf TA, Sugawara Y, Baumberg JJ (2006) Opt Express 14(5):1965
24. Lacharmoise PD, Tognalli NG, Goñi AR, Alonso MI, Fainstein A, Cole RM, Baumberg JJ, García de Abajo FJ, Bartlett PN (2008) Phys Rev B 78(12):125410
25. Baumberg JJ, Kelf TA, Sugawara Y, Cintra S, Abdelsalam ME, Bartlett PN, Russell AE (2005) Nano Lett 5(11):2262
26. Cintra S, Abdelsalam ME, Bartlett PN, Baumberg JJ, Kelf TA, Sugawara Y, Russell AE (2006) Faraday Discuss 132:191. doi:10.1039/b508847j
27. Tognalli NG, Cortés E, Hernández-Nieves AD, Carro P, Usaj G, Balseiro CA, Vela ME, Salvarezza RC, Fainstein A (2011) ACS Nano 5(7):5433. doi:10.1021/nn200567m

28. Mahajan S, Cole RM, Soares BF, Pelfrey SH, Russell AE, Baumberg JJ, Bartlett PN (2009) J Phys Chem C 113(21):9284. doi:10.1021/jp900661u
29. Tognalli N, Fainstein A, Calvo E, Abdelsalam M, Bartlett P (2012) J Phys Chem C 116(5):3414–3420. doi:10.1021/jp211049u
30. Cortés E, Tognalli NG, Fainstein A, Vela ME, Salvarezza RC (2009) Phys Chem Chem Phys 11(34):7469. doi:10.1039/b904685m
31. Tognalli NG, Scodeller P, Flexer V, Szamocki R, Ricci A, Tagliazucchi M, Calvo EJ, Fainstein A (2009) Phys Chem Chem Phys 11(34):7412. doi:10.1039/b905600a
32. Scodeller P, Flexer V, Szamocki R, Calvo EJ, Tognalli NG, Troiani H, Fainstein A (2008) J Am Chem Soc 130(38):12690. doi:10.1021/ja802318f
33. Abdelsalam ME, Bartlett PN, Russell AE, Baumberg JJ, Calvo EJ, Tognalli NG, Fainstein A (2008) Langmuir 24(13):7018. doi:10.1021/la800410x
34. Mahajan S, Richardson J, Brown T, Bartlett PN (2008) J Am Chem Soc 130(46):15589. doi:10.1021/ja805517q
35. Lindquist NC, Luhman WA, Oh S, Holmes RJ (2008) Appl Phys Lett 93(12):123308. doi:10.1063/1.2988287
36. Dunbar R, Hesse H, Lembke D, Schmidt-Mende L (2012) Phys Rev B 85(3):1. doi:10.1103/PhysRevB.85.035301
37. Kim SI, Imura K, Kim S, Okamoto L (2011) J Phys Chem C 115:1548–1555
38. Okamoto K, Lončar M, Yoshie T, Scherer A, Qiu Y, Gogna P (2003) Appl Phys Lett 82(11):1676. doi:10.1063/1.1559646
39. Mooradian A (1969) Phys Rev Lett 22(5):185. doi:10.1103/PhysRevB.65.075419
40. Fox M (2001) Optical properties of solids. Oxford University Press, Oxford
41. Okamoto H, Imura K (2008) Jpn J Appl Phys 47(7):6055. doi:10.1143/JJAP.47.6055
42. Goñi AR, Güell F, Perez LA, Lopez-Vidrier J, Ossó JO, Coronado EA, Morante JR (2012) Nanoscale 4:1620
43. Romero I, Teperik TV, García de Abajo FJ (2008) Phys Rev B 77(12):125403
44. Romero I, García de Abajo FJ (2009) Opt Express 17(21):18866